Ultrahigh-Performance ENZ Modulator Based on a Stack of Three-Layer Graphene and ITO

Mohsen Heidari, Shahram Bahadori-Haghighi, Babak Janjan, Mohammad R. Khosravi, and Derek Abbott, *Fellow, IEEE*

***Abstract*—A high-performance electro-absorption optical modulator based on the epsilon-near-zero (ENZ) effect is proposed. The structure consists of a waveguide with a silicon (Si) core over which a stack of graphene/HfO_2/graphene/ITO/HfO_2/graphene is grown, covered by a Si cladding. An external voltage is applied across the graphene layers to change the carrier concentration in the indium tin oxide (ITO) layers. Using a self-consistent theory, the required voltage to achieve the ENZ points in the ITO layers is calculated up to 3.42 V for an ITO thickness of 5 nm. The operation of the modulator is investigated using a three-dimensional finite-difference time-domain (FDTD) method, resulting in a modulation depth as high as 5.23 dB/μm (5.36 dB/μm) at a wavelength of 1.55 μm for the TE (TM) polarization, which ensures the polarization-insensitivity of our proposed modulator. It is also calculated that the insertion loss of the modulator is in the order of 2.5×10^{-3} dB/μm that yields the figure of merit (FOM) of more than 1800. The outstanding features of our proposed modulator are mainly attributed to using the Si cladding layer instead of metal cladding. Furthermore, in contrast to the previously studied structures with metal electrodes, graphene layers significantly reduce the insertion loss.**

***Index Terms*—Indium tin oxide, graphene, quantum capacitance, high-performance modulator.**

I. Introduction

THE influx of high-bandwidth applications necessitates high-speed on-chip interconnects in optical communication systems. The optical modulator is one of the key components for optical communication networks that is used to modify the characteristics of an optical carrier such as its amplitude, phase or polarization. Various types of optical modulators based on the electro-optic [1]–[3], electro-absorption (EA) [4], [5]. thermo-optic [6], [7] and magneto-optic [8] effects have already been investigated.

Manuscript received December 22, 2020; revised August 4, 2021; accepted August 25, 2021. Date of publication September 3, 2021; date of current version September 15, 2021. (*Corresponding author: Mohsen Heidari.)*

Mohsen Heidari and Babak Janjan are with the School of Electrical and Computer Engineering, Tarbiat Modares University, Tehran 14115-111, Iran (e-mail: mh.heidari@modares.ac.ir; b.janjan@modares.ac.ir).

Shahram Bahadori-Haghighi is with the School of Electrical and Computer Engineering, Shiraz University, Shiraz 71348-51154, Iran (e-mail: sbahadori@shirazu.ac.ir).

Mohammad R. Khosravi is with the Department of Electrical and Electronics Engineering, Shiraz University of Technology, Shiraz 71555-313, Iran (e-mail: m.khosravi@sutech.ac.ir).

Derek Abbott is with the School of Electrical and Electronic Engineering, The University of Adelaide, Adelaide SA 5005, Australia (e-mail: derek.abbott@adelaide.edu.au).

Color versions of one or more figures in this article are available at https://doi.org/10.1109/JSTQE.2021.3108461.

Digital Object Identifier 10.1109/JSTQE.2021.3108461

Silicon (Si) electro-optic modulators have been of great interest as they are compatible with the complementary metal-oxide semiconductor (CMOS) technology. Silicon modulators are typically based on the free-carrier plasma dispersion effect whereby the refractive index of Si is changed and phase modulation of the propagating light is performed. In the previously studied Si modulators, the phase variation is usually converted to the amplitude modulation of light using Mach-Zehnder interferometers (MZIs) [9]–[11]. However, such Si modulators suffer from large footprints and low modulation efficiency due to the weak plasma dispersion effect in Si [12]. Therefore, new effective materials such as transparent conductive oxides (TCOs) and graphene have always been explored to realize high-performance miniaturized optical modulators.

TCOs are a specific class of materials which have recently attracted much attention to increase the modulation efficiency and reduce the size of the modulators. The permittivity of the TCOs can be effectively tuned by applying an external bias and changing their carrier density. When the carrier concentration changes, the real part of the permittivity in TCOs can cross zero at a specific wavelength that is known as the epsilon-near-zero (ENZ) effect. As a result, light can be tightly confined into the sub-wavelength scales and the resultant high intensity enhances light-matter interaction. Various optical modulators using indium tin oxide (ITO) as a well-recognized TCO have been studied by many researchers [13]–[16]. The most popular structures are based on hybrid plasmonic waveguides (HPWs) where the ITO and its adjacent oxide are inserted between metal and Si layers in order to apply the external voltage. ITO hybrid plasmonic modulators with the extinction ratios of more than 1 dB/μm have previously been proposed [13], [14]. In 2018, an EA ITO modulator with an extinction ratio of 6.5 dB and insertion loss of 10 dB over a 4 μm HPW was experimentally demonstrated [17]. A modulation depth of as high as 19.9 dB over a HPW length of just 1 μm has also been presented [18]. It is reported that the applied voltage changes between -2 to 4 V. Although a modulation speed of as high as 11 GHz can be obtained the propagation loss is as high as 3 dB. Therefore, it is obvious that hybrid plasmonic structures suffer from high insertion loss. Instead, when the TCO is sandwiched between two Si layers to form a slot waveguide, low propagation loss is expected. An optical modulator based on a Si slot waveguide and aluminum-doped zinc oxide (AZO) as the TCO has been proposed whereby a modulation depth of 3 dB and insertion loss of just 0.69 dB over a length of 250 nm have been achieved [19].

In 2019, an ITO modulator using a 10 μm dual-slot Si waveguide was proposed based on which a high extinction ratio of 14.4 dB and low insertion loss of 0.37 dB were obtained [20]. However, it should be noted that in optical modulators based on slot waveguides, the Si layers are required to be doped for serving as the electrodes and it will introduce extra insertion loss that is not desirable.

Another promising material that has revolutionized different electronic and optical devices is graphene. Graphene is a two-dimensional (2D) array of carbon atoms that possesses intriguing electrical, thermal and optical properties. In recent years, various graphene-based optical devices such as photodetectors [21], [22], polarizers [23], [24], mode-locked laser [25], optical switches and modulators [26]–[30] have been investigated. The graphene characteristics can be greatly tuned by applying an external voltage that is very promising for active optical devices such as modulators. Furthermore, the high carrier mobility of graphene reported [31], [32] is highly desirable for realization of high speed optical modulators. Graphene can also exhibit high optical absorption over a broad spectrum from visible to infrared. On the other side, graphene-based structures are generally CMOS compatible [33] so that implementation of ultra-compact optical modulators is attainable.

Several kinds of graphene-based EA modulators have been reported. In 2011, the first prototype of a graphene Si EA modulator was experimentally demonstrated whereby a modulation depth of 4 dB and bandwidth of 1 GHz over a 40 μm long waveguide were obtained [34]. The modulation is performed through tuning the Fermi level of graphene by applying a voltage across the doped Si waveguide and graphene. In order to eliminate the extra insertion loss introduced by the doped Si back, double-layer graphene optical modulators have been proposed where the external voltage is applied between the two graphene layers. A modulation depth of 6.5 dB over a Si waveguide length of 40 μm at a drive voltage of 5 V has been achieved by a double-layer graphene modulator [35]. In 2016, a high speed 35 GHz double-layer graphene modulator with a modulation depth of 2 dB and low insertion loss of 0.9 dB was experimentally investigated too [36]. However, the required voltage was obtained to be as high as 25 V for a waveguide length of 30 μm. In some other optical modulators, graphene has been incorporated into the resonators to enhance light-graphene interaction. A modulation depth of 40% has been achieved by applying a tuning voltage of 6 V to a modulator made by graphene on a Si microring resonator [37]. However, such resonant structures will definitely limit the operating spectral range of the modulator.

It should be mentioned that most of the previously reported modulators based on the tunable materials such as TCOs and graphene are polarization-sensitive that imposes some limitation in practical applications. This is due to that some devices like polarizers, polarization controllers or polarization-maintaining fibers are required to align the polarization of light with the polarization-sensitive modulators. There is no doubt that in such cases the coupling and propagation loss of the system will increase. Therefore, design and implementation of polarization-independent modulators are desirable. A polarization-independent EA ITO modulator has already been proposed based on which the modulation depth of 19.9 and 15.2 dB has been obtained for transverse electric (TE) and transverse magnetic (TM) modes, respectively [18]. A polarization-insensitive graphene-based modulator using a 10.35 μm-long Si waveguide exhibiting a limited modulation depth of 3 dB for both the TE and TM polarized modes has also been studied [38]. In 2019, a graphene-based EA modulator with a length of 20 μm was proposed where a high modulation depth of more than 22 dB was obtained at the wavelength of 1.55 μm for both polarizations [39]. The modulation was performed over a broad spectral width of more than 300 nm.

In this paper, we present a very high-performance EA modulator with outstanding characteristics. In fact, a waveguide modulator is proposed that is based on an attractive combination of both the ITO and graphene layers as the well-known effective materials. The structure consists of three graphene sheets spaced by thin HfO_2 and ITO layers which are all grown over a Si waveguide. The thickness of the ITO layer is considered to be 5 nm is feasible with current fabrication technologies [40], [41]. In contrast to the previously studied similar modulators with metal clads [17], [18], [42], the proposed structure is covered by a Si dielectric clad which causes enhanced modulation efficiency without any additional losses. The state of the modulator is changed by the carrier accumulation and depletion in the graphene and ITO layers. In addition, the graphene layers play the roles of electrodes for adjusting the carrier concentration of ITO to the ENZ point. In Section 2, the optical characteristics of the ITO at different carrier concentrations are investigated. The electrical characteristics of the structure is also studied in Section 3 where the quantum capacitance of graphene is calculated based on the self-consistent theory. It is presented that the required voltages to obtain the ENZ point at the ITO layer is as low as 1.75 and 3.42 V corresponding to the accumulation layer (AcL) thicknesses of 1 and 2 nm, respectively. In Section 4, the mode analysis and the 3D simulation of the proposed modulator are accomplished using the finite-difference time-domain (FDTD) method. According to the presented results, a very high modulation depth of more than 5.23 dB/μm (5.35 dB/μm) is obtained for the TE (TM) modes which confirms the polarization-insensitivity of our proposed modulator. The corresponding insertion loss of 2.64×10^{-3} dB/μm (2.8×10^{-3} dB/μm) for both the polarization modes is precisely calculated based on the 3D-FDTD simulations. It is interesting that according to the illustrated results, the structure exhibits a figure of more than 1800 that is two orders of magnitude larger than those in the previously studied EA modulators. A very high 3 dB bandwidth of 4.5 GHz is estimated that is really promising for fast optical communication networks. Finally, a summary of the results and conclusions is provided in Section 5.

II. Modulator Structure

The 3D schematic of the proposed graphene-ITO EA modulator is shown in Fig. 1(a). The cross-section view of the structure is also shown in Fig. 1(b) where the geometrical parameters are indicated. As it is shown, the modulator consists of a Si

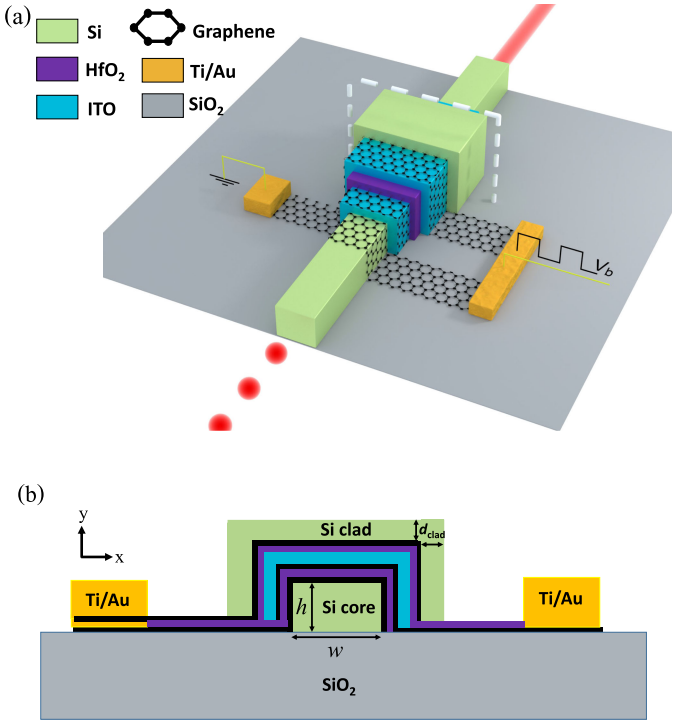

Fig. 1. Graphene-ITO ENZ modulator. (a) The perspective view and (b) the cross-section view of the proposed graphene-ITO modulator.

ridge waveguide with a width of w and height of h that can be made from a standard silicon-on-insulator (SOI) platform. The waveguide structure is covered by three graphene sheets which are spaced by two thin HfO_2 and an ITO layer as shown in Fig. 1(b). As a result, a stack of graphene/HfO_2/graphene/ITO/HfO_2/graphene is deposited on the silicon waveguide. The whole structure is then covered by a Si clad layer as shown in Fig. 1.

As it can be seen in Fig. 1(b), the ITO layer together with its adjacent thin HfO_2 layers are sandwiched by graphene sheets forming an oxide capacitor. The titanium-gold stack (Ti/Au) electrodes (with the thickness of 5/50 nm) are located on the two sides of the structure that are 1 μm away from the silicon waveguide to avoid any undesirable effects on the optical mode. The right Ti/Au electrode is in direct contact with the middle graphene layer which forms one plate of the asymmetric oxide capacitor while the left electrode is connected to the top and bottom graphene sheets which play the role of the second plate of the oxide capacitor.

The external voltage source can be applied to the aforementioned oxide capacitor through the Ti/Au electrodes. In the oxide capacitor, the graphene sheets play the roles of gating electrodes to change the carrier concentration in the ITO layer. The thin HfO_2 layers serve as high-κ gate dielectrics. The interaction between the propagating light and the active graphene and ITO layer determines the state of the modulator.

In order to gain more insight into the modulation performance of the structure, the behavior of the ITO should be taken into consideration. When a voltage is applied between the middle and the top/bottom graphene sheets (with the positive polarity

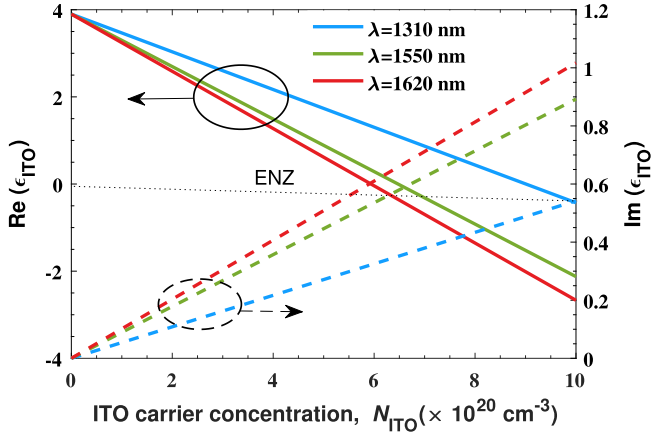

Fig. 2. ITO Characteristics. The calculated real and imaginary parts of the permittivity of ITO versus the carrier concentration at three different wavelengths.

applied to the top/bottom graphene layers), the electrons are accumulated inside the ITO layer so that its dielectric constant changes. The ITO dielectric constant is obtained according to the Drude model [18] as:

$$\varepsilon = \varepsilon_\infty - \frac{N_{\rm ITO} e^2}{\varepsilon_0 m^*} \cdot \frac{1}{\omega^2 + i\omega\Gamma} \tag{1}$$

where ε_∞ is the high-frequency permittivity, $N_{\rm ITO}$ is the electron concentration, e is the electron charge, ε_0 is the permittivity of free space, m^* is the effective mass, ω is the angular frequency of light and Γ is the damping factor of electron.

By changing the electron concentration, the real and imaginary parts of the dielectric constant and as a result the associated absorption and refractive index of ITO change accordingly. Assuming the high-frequency permittivity of $\varepsilon_\infty = 3.9$, damping factor of $\Gamma = 1.8 \times 10^{14}$ s^{-1} [18] and effective mass of $m^* = 0.35 m_e$ (where m_e is the electron mass) [43], the real and imaginary parts of the dielectric constant of ITO as functions of the carrier concentration at different wavelengths are calculated and shown in Fig. 2. As it is expected, the imaginary part of the permittivity increases by increasing the carrier concentration in ITO. On the other side, when the electron density increases, the real part of the dielectric constant decreases so that it crosses zero at a specific concentration that is called the ENZ point. As it can be seen, the ENZ point at the wavelength of 1550 nm is obtained when the carrier concentration is 6.48×10^{20}cm^{-3}. The ENZ point at longer wavelengths is achieved by lower carrier concentration. At this point, the ITO transforms from a dielectric to a quasi-metal material. The ENZ point is of great importance in our proposed modulator. When the real part of the permittivity is close to zero, the light is strongly confined within the ITO layer because of the continuity of the normal electric displacement fields at the interfaces. As a result, the light-matter interaction is remarkably enhanced that is favorable to realize an efficient optical modulator [12], [44]. Tuning the carrier density of ITO near the ENZ point plays a critical role in the modulation of the propagating light. The required voltage to achieve the ENZ carrier concentration is calculated in the following section.

III. Electrical Characteristic

A. ENZ Voltage

The required electrical voltage is one of the most important characteristics of electro-optic or electro-absorption modulators. As it was mentioned in the previous section, the optical modulation of our proposed modulator is performed by applying a voltage between the middle and top/bottom graphene sheets to change the carrier concentration of the ITO layer. The state of the modulator is changed by adjusting the carrier concentration of ITO to the ENZ point. The required voltage to achieve the desired ITO carrier density of N_{ITO} is obtained from the following relation:

$$V = \frac{eN_{\mathrm{ITO}}}{C_T} + \frac{\Delta\mu}{e} \tag{2}$$

where C_T is the total capacitance of the proposed structure that is connected to the Ti/Au electrodes, and $\Delta\mu$ is the total shift of chemical potentials of this three-layer graphene system. As it can be seen in Fig. 1(b), the right Ti/Au electrodes are connected to the top and bottom graphene layers while the left electrode is connected to the middle graphene sheet. Therefore, an asymmetrical parallel-plate capacitor is formed so that one plate consist of a stack of ITO/middle graphene layer and the other plate consists of the connection of two layers of top and bottom graphene sheets. In addition to the parallel-plate oxide capacitance, quantum capacitance associated to the graphene layers should be taken into account. As it is known, the quantum capacitance of graphene (which is related to the density of states of carriers) is usually large enough so that its effect on the total capacitance of the structure can be ignored. However, in recent high performance optical and electrical devices, thin oxide layers with high dielectric constants are required to decrease the operating gating voltages. In such cases, the parallel-plate capacitance is large and the quantum capacitance could not be ignored anymore. In our proposed modulator, the quantum capacitance should also be taken into account due to the small thicknesses of the ITO and thin HfO_2 layers between the graphene sheets. The total capacitance of the structure is the series combination of the oxide or electrostatic capacitance (C_{ES}) and quantum capacitance (C_Q). The quantum capacitance of an ideal graphene layer can be calculated as [45]:

$$C_Q = \frac{2e^2 k_B T}{\pi(\hbar v_F)^2} \ln\left[2\left(1+\cosh\frac{\mu}{k_B T}\right)\right] \tag{3}$$

According to the experimental measurements and as it is previously discussed [45], the minimum of the quantum capacitance is nonzero. This is due to the defects and impurities that exist in a real graphene sheet. The impurities result in charge centers and consequently potential fluctuations in graphene. According to the self-consistent theory, the potential fluctuations yield an additional carrier density n^* so that the total carrier density is expressed as follows [45]:

$$n = |n_G| + |n^*| \tag{4}$$

where n_G is the carrier density induced by the applied gate voltage and n^* is the carrier density due to charged impurities.

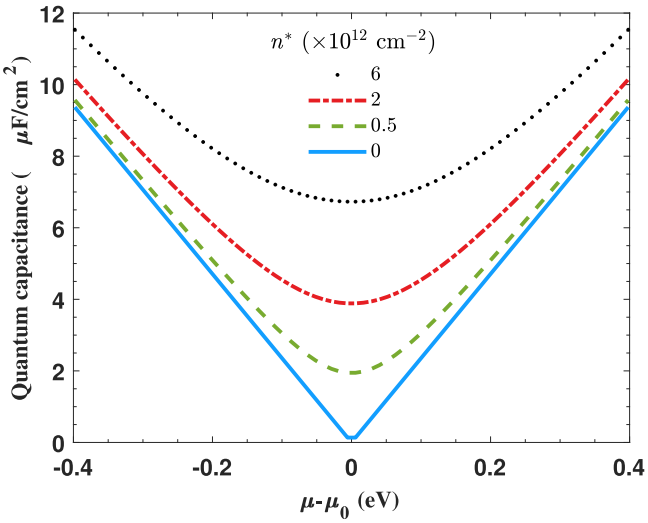

Fig. 3. Quantum capacitance of graphene as a function of the chemical potential and doping concentration, n^* (0, 0.5, 2 and 6 $\times 10^{12}$ cm^{-2}).

As a result, the quantum capacitance is calculated as:

$$C_Q = \frac{2e^2}{\hbar v_F \sqrt{\pi}} \sqrt{|n_G| + |n^*|} \tag{5}$$

It should be mentioned that the above model based on the self-consistent theory can be used to take into account the doping of the graphene sheets in our proposed structure before applying the external gate voltage. The calculated quantum capacitance of graphene as a function of the chemical potential for various doping concentrations is plotted in Fig. 3. As it is expected, the minimum of the quantum capacitance is nonzero for an n-doped graphene layer while it would be zero when there is no doping. The contribution of the doping concentration to the chemical potential of graphene is taken as μ_0. Another interesting point is that the higher doping concentration result in the larger quantum capacitance. This is due to the fact that the quantum capacitance is related to the density of states of graphene that increases with the chemical potential. It means that applying a gate voltage to the graphene layer with larger chemical potential could induce higher carrier density in graphene because higher density of states is available to be filled by electrons.

According to the above discussion, the required gate voltage to achieve the ENZ point in the ITO layer of the proposed modulator can now be calculated. In addition to the quantum capacitance, the parallel-plate oxide capacitance or in other words the electrostatic capacitance $C_{\mathrm{ES}} = \varepsilon_r / d_{\mathrm{ox}}$ should be calculated where ε_r and d_{ox} are the dielectric constant and thickness of the thin dielectric layers adjacent to the ITO, respectively. Using the self-consistent theory and Eq. 5, the required voltage to induce desired ITO carrier concentration as a function of the electrostatic capacitance is calculated and shown in the color plots of Fig. 4. The thicknesses of the accumulation layers at the top/bottom of the ITO layer is taken as $t_{\mathrm{AcL}} = 1$ nm and 2 nm in Figs. 4(a) and (b), respectively. In order to make the color plots more readable, black dotted curves corresponding to the voltages of 2 and 5 V are indicated. According to Fig. 4, it is obvious that specific ITO carrier concentrations like the ENZ points

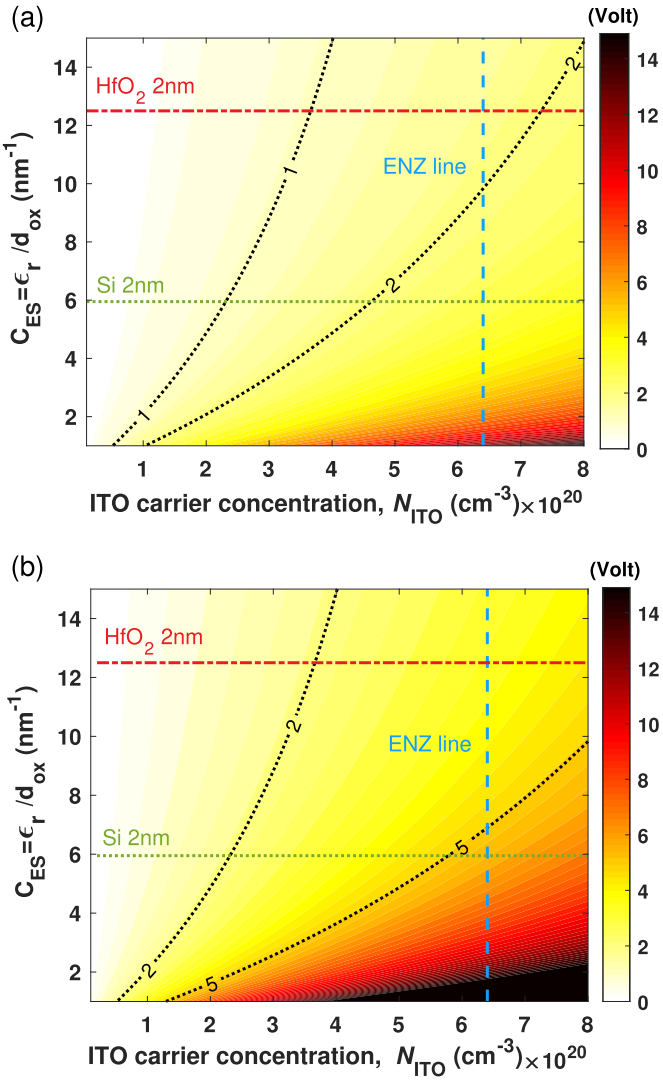

Fig. 4. Drive voltage of the modulator. The required gate voltages as functions of the electrostatic capacitance and the induced ITO carrier concentrations for (a) $t_{\mathrm{AcL}} = 1$ nm and (b) $t_{\mathrm{AcL}} = 2$ nm.

corresponding to the vertical blue dashed lines are obtained by lower gating voltages when the oxide capacitance is larger. The dielectrics adjacent to the ITO layer can play important roles to achieve a large parallel-plate capacitance. Obviously, the dielectrics with higher dielectric constants ε_r result in larger oxide capacitance and consequently lower ENZ voltages. The horizontal green dotted and red dash dotted lines indicate the electrostatic capacitance corresponding to the 2 nm Si and HfO_2 dielectric layers adjacent to the ITO, respectively. According to Fig. 4(a), the required ENZ voltage for $t_{\mathrm{AcL}} = 1$ nm is 2.78 V when Si is used as the thin dielectric layer while it is 1.75 V when the dielectric layer is HfO_2. Therefore, our proposed modulator with the thin HfO_2 dielectric layers is more advantageous than that with Si dielectric layers. As it is shown in Fig. 4(b), the required ENZ voltages are 5.52 V and 3.42 V for Si and HfO_2 as the dielectric layers, respectively, when $t_{\mathrm{AcL}} = 2$ nm. Clearly, the thicker ITO layer requires much larger voltages to achieve the ENZ carrier concentrations. However, the AcL thickness of

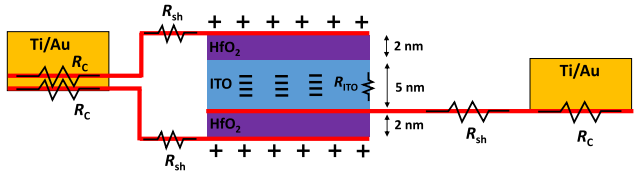

Fig. 5. The equivalent circuit of the device and the schematic of the three-layer graphene and ITO stack connected to the metal contacts with the associated resistances.

2 nm is selected because higher light-matter interaction and as a result modulation depth is expected.

Regarding the fabrication process, note that although deposition of a high quality and continuous ITO layer below 2 nm is technically challenging, our proposed ITO thickness is 5 nm and there are some references where high quality ITO films thinner than 5 nm have been grown using standard RF sputtering [40], [41]. In addition, the deposition of ultrathin layer of HfO_2 below 2 nm is also feasible and this is reported in many previous studies where ABC metamaterials with ultrathin layers of HfO_2 have been fabricated [46]. In this regard, the ITO and HfO_2 thicknesses have also fabrication tolerances because on one side, the variation of ITO thickness has no effect on the oxide capacitance of the structure and hence, has no effect on the formation of the 1–2 nm accumulation layer inside the ITO. On the other side, the variation of the HfO_2 thickness directly affects the oxide capacitance of the structure. However, any changes in the HfO_2 thickness and hence in the oxide capacitance can be translated as a change in the required voltage to form the accumulation layer.

Another important point is that the accumulation layer that is formed at the middle of the ITO (due to the symmetry of the structure) is calculated based on Thomas-Fermi screening theory [43] so that for low bias voltages of about 1–1.5 V, the thickness of accumulation layer is about 1 nm. For higher bias voltages of about 3–5 V, the calculated accumulation layer thickness is almost 2 nm.

B. Modulation Bandwidth

At the end of this section, the 3 dB bandwidth of the structure can be estimated. As it is known, the modulation speed is mainly limited by the RC time constant of the structure. In order to gain a good insight into the bandwidth calculations, the stack configuration of the graphene and ITO layer with the metal contacts is schematically shown in Fig. 5. The contact and sheet resistances of the graphene layers and also the ITO resistances are all shown in Fig. 5. It should be mentioned that the middle graphene sheet with its adjacent ITO layer play the role of one plate of the oxide capacitance with HfO_2 as the dielectrics. As it is seen in Fig. 5, the top and bottom graphene layers are connected to the same potential which form the second plates of the oxide capacitance. Therefore, it can be assumed that there are two parallel oxide capacitors with the plates of the top/bottom and middle graphene layers. However, the quantum capacitance that are in series connection with the oxide capacitance, should also be taken into account. According to Eq. 5, the quantum

capacitance per unit area is in the order of 6.73 μ F/cm ^{2}. Assuming that the length and width of the waveguide are 3 μm (modulator length) and 960 nm (i.e. $2h + w$), respectively, the quantum capacitance of the graphene layers are approximately 193.8 fF. On the other hand, the oxide capacitance are calculated to be ∼318 fF. As a result, the total capacitance of the structure is 240 fF.

In order to obtain the bandwidth of the modulator, the ohmic resistances of the structure should also be investigated. According to Fig. 5, there are contact and sheet resistances attributed to each of the top, bottom and middle graphene layers. It is obvious that the top and bottom graphene layers are connected to the left metal electrode. The other sides of the top and bottom graphene sheets (connected to the HfO_2 layers) must be at the same potential due to the symmetry of the structure. As a result, it can be assumed that the top and bottom graphene layers and consequently their associated contact and sheet resistances are parallel with each other. On the other side, the ITO resistance will be in series with the sheet and contact resistances of the middle graphene layer. In order to obtain the sheet and contact resistances of the graphene layers, we refer to the corresponding values reported in previous works. The graphene sheet resistance, $R_{\rm sh}$ is typically 100-300 $\Omega/\square$ [47], [48] and the contact resistance, R_c is in the range of 100–1000$\Omega\cdot\mu$m depending on the specific metal and fabrication processes [48], [49]. Assuming a sheet resistance of 200 $\Omega/\square$ and a contact resistance of 400 $\Omega\cdot\mu$m, the total ohmic resistance of 350 Ω is obtained for the structure. It should be mentioned that in the calculation of the sheet resistances, it is assumed that the metal contacts are 1 μm away from the waveguide core. Finally, according to the calculated parameters, the 3 dB bandwidth of more than 4.5 GHz is expected that is acceptable.

C. Chemical Potential Engineering

The chemical potential variations of the three graphene layers as the plates of the capacitor versus the bias voltage (V_b) are shown in Fig. 6(a). As it can be seen, when the bias voltage is applied, the bottom/top graphene sheets are doped by holes while the middle graphene is doped by electrons or vice versa so that the chemical potentials of the bottom/top (μ_1/μ_3) and middle (μ_2) graphene layers shift in the opposite directions. Therefore, as the bias voltage increases, μ_2 increases while μ_1 and μ_3 decrease. The real and imaginary parts of the permittivity and the absolute value of the refractive index of graphene as a function of the chemical potential at $\lambda = 1550$ nm is depicted in Fig. 6(b). As it is shown, graphene becomes a very lossy material when its chemical potential is below 0.4 eV ($|\mu| \leq 0.4$ eV) corresponding to the transparent red region in Fig. 6(b). On the other side, the imaginary part of the permittivity is almost zero for $|\mu| \geq 0.5$ eV corresponding to the transparent blue region in Fig. 6(b) where graphene can be considered as a very low-loss material. When the modulator operates in the on-state (i.e. with low insertion loss corresponding to $V_b = 0$), both the graphene and ITO layer should result in low losses. Thus, the chemical potentials of the graphene layers should be grater than 0.5 eV for lossless operation. In this regard, we choose the initial chemical potential

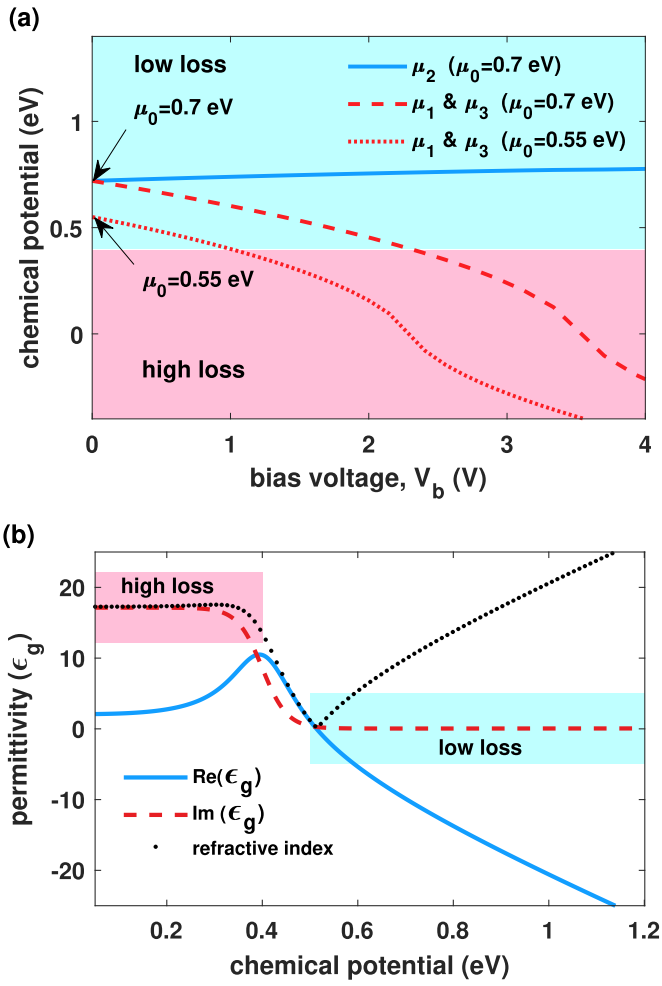

Fig. 6. Loss engineering of the three graphen layers. (a) The chemical potential of three graphene layers constructing the capacitor as a function of bias voltage. As the bias voltage exceeds 2 V for $\mu_0 = 0.7$ eV (1 V for $\mu_0 = 0.55$ eV) the bottom and top graphene layers (μ_1 and μ_3) enter the high-loss region. (b) The high-loss and low-loss region of graphene versus its chemical potential.

of $\mu_0 = 0.7$ eV for all the three graphene layers. In contrast, both graphene and ITO should be very lossy for the off-state operation of the modulator so that a synergistic effect is achieved. As can be seen in Fig. 6(a), when the bias voltage exceeds 2 V for the case of $\mu_0 = 0.7$ eV (1 V for the case of $\mu_0 = 0.55$ eV) the top/bottom graphene layers enter the high-loss region. It should be mentioned that in order to reach the high-loss region at a lower bias voltage specially for $t_{\rm AcL} < 2$ nm, the initial chemical potentials of the top/bottom graphene layers can be set as ($\mu_3 = \mu_1 = 0.55$ eV) that are different from that of the middle graphene layer ($\mu_2 = 0.7$ eV). Interestingly, the main advantage of graphene over noble metals is that its associated loss can be adjusted so that it can operate in both the low-loss (at $V_b = 0$ V) and high-loss (at $V_b = 3.42$ V) modes. As a result, very low and high insertion loss is achieved respectively in the on- and off-states of the modulator and consequently a very high FOM is attained.

At the end of this section it should also be mentioned that various double layer graphene optical modulators have already

been investigated. However, according to Fig. 5, in our proposed structure with three graphene sheets, top/bottom capacitor (plate#1: top/bottom graphene sheet, plate#2: the middle graphene and ITO layer, oxide: top/bottom oxide layer) contain a certain amount of charge, say Q_1. Hence, the total accumulated charge carrier in the common plate (middle graphene sheet and ITO layer) becomes $2 \times Q_1$. Thus, for a specific applied voltage, the accumulated charges at the common middle plate (inside ITO and graphene) are raised by a factor of 2. Therefore, in our proposed configuration, we can use a half drive voltage to obtain a certain amount of accumulated charge in comparison to the configuration with two graphene sheets and this is the advantage of our stack.

IV. Results and Discussion

The operation of the modulator is investigated using the 3D FDTD method where the computational cell is totally surrounded by perfectly matched layers (PMLs). The mesh size around the graphene layer is reduced down to 0.1 nm along the y-axis. The refractive index of the ITO layer is obtained from Eq. 1. The dielectric constants of the graphene layers are also calculated as follows:

$$\varepsilon_g(\omega) = 1 + \frac{j\sigma(\omega)}{\omega\varepsilon_0\Delta} \tag{6}$$

where Δ is the effective thickness of the graphene sheet that is taken to be 0.34 nm and σ is the complex conductivity of graphene. The complex conductivity is determined by the Kubo formalism as follows:

$$\sigma(\omega) = \frac{je^2\mu}{\pi\hbar^2\left(\omega + j\tau^{-1}\right)} + \frac{je^2}{4\pi\hbar}\ln\left(\frac{2\left|\mu\right| - \hbar\left(\omega + j\tau^{-1}\right)}{2\left|\mu\right| + \hbar\left(\omega + j\tau^{-1}\right)}\right) \tag{7}$$

where τ is the relaxation time that is calculated as $\tau = \frac{\mu_e\mu}{ev_F^2}$ with the carrier mobility of μ_e=10000 cm^2 V^{-1} s^{-1} [50].

The propagation loss of the TE and TM modes ($\alpha_{\rm TE}$ and $\alpha_{\rm TM}$) of the proposed modulator is calculated versus the ITO carrier concentration that is shown in Fig. 7(a). As the operation of the modulator can be affected by the geometrical parameters, the propagation loss is calculated for two different Si core widths $w = 320$ and 380 nm and two heights $h = 240$ and 290 nm. The operating wavelength is also set as $\lambda = 1550$ nm. As it is shown in Fig. 7(a), $\alpha_{\rm TE}$ and $\alpha_{\rm TM}$ increase up to a maximum value by increasing the ITO carrier density. In fact, when the carrier concentration of ITO increases, it moves toward a metal-like material until it reaches the ENZ point. It is obvious that the maximum propagation loss is achieved around the ENZ carrier concentration of $6.48 \times 10^{20}\text{cm}^{-3}$. This is due to the strong light confinement inside the ITO layer as a result of the small dielectric constant of ITO at the ENZ point. Therefore, the ENZ point where the TE (TM) propagation loss is as high as 0.935 dB/μm (0.95 dB/μm) is considered to be the off-state of the modulator because the output optical power is low. On the other side, it can be seen that at low ITO carrier concentration, the propagation loss is much lower than that at the ENZ point so that the modulator is in the on-state. It should also be noted that the propagation loss is reduced by further increasing $N_{\rm ITO}$ from

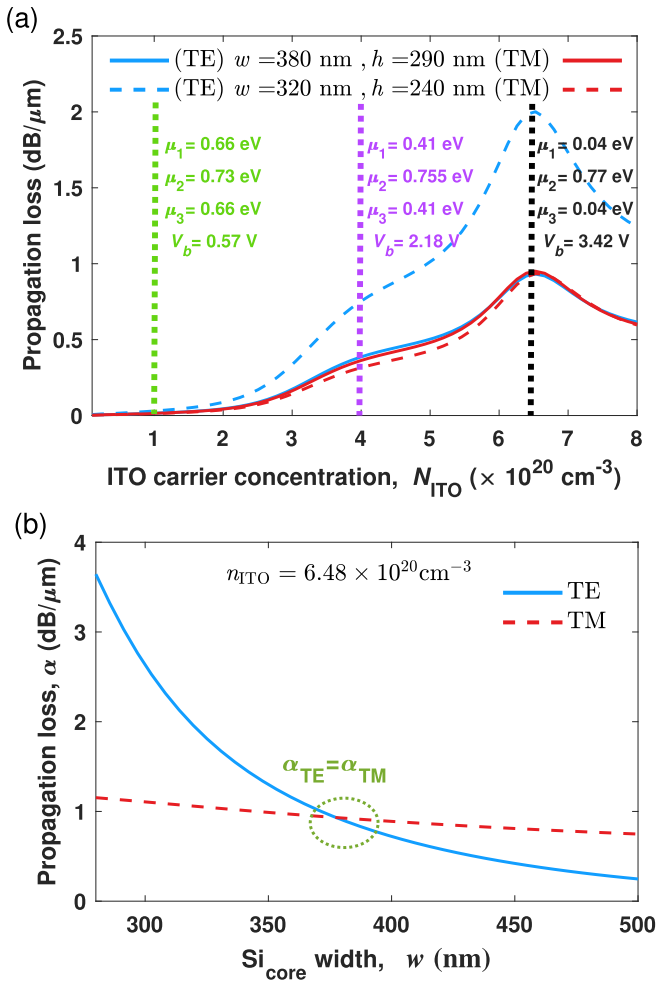

Fig. 7. (a) The calculated $\alpha_{\rm TE}$ and $\alpha_{\rm TM}$ of the proposed modulator as functions of the ITO carrier concentration at two different core sizes. (b) The calculated $\alpha_{\rm TE}$ and $\alpha_{\rm TM}$ of the proposed modulator as functions of the Si core width at the ITO carrier concentration of $N_{\rm ITO} = 6.48 \times 10^{20}\text{cm}^{-3}$.

the ENZ carrier concentration because the ENZ effect and the strong light-matter interaction no longer exist. Hence, the high ITO carrier concentration (i.e. $N_{\rm ITO} \gg 6.48 \times 10^{20}\text{cm}^{-3}$) can also be considered as the on-state. Therefore, the modulation of light is performed by changing the ITO carrier density either from $N_{\rm ITO} \ll 6.48 \times 10^{20}\text{cm}^{-3}$ to $N_{\rm ITO} = 6.48 \times 10^{20}\text{cm}^{-3}$ that is defined as the accumulation mode or from $N_{\rm ITO} \gg 6.48 \times 10^{20}\text{cm}^{-3}$ to $N_{\rm ITO} = 6.48 \times 10^{20}\text{cm}^{-3}$ that is called the depletion mode. However, the modulation depth that can be achieved in the accumulation mode is higher than that in the depletion mode as it is seen in Fig. 7(a). As it is shown in Fig. 7(a), for the core width and height of $w = 380$ nm and $h = 290$ nm, the TE (TM) modulation depth of 0.932 dB/μm (0.947 dB/μm) is achieved in the accumulation mode by changing $N_{\rm ITO}$ from $1 \times 10^{19}\text{cm}^{-3}$ to the ENZ point. It is while in this case, the TE (TM) modulation depth by changing $N_{\rm ITO}$ from $8 \times 10^{20}\text{cm}^{-3}$ to the ENZ point in the depletion mode is 0.32 dB/μm (0.35 dB/μm).

According to Fig. 7(a), it is interesting that the propagation loss of the TE polarization is affected by the geometrical parameters. It should be noted that the propagation loss is nearly

the same for both the TE and TM propagating modes in the off- and on-states for the core width and height of $w = 380$ nm and $h = 290$ nm so that their corresponding modulation depth is almost equal. Therefore, the polarization-insensitivity of our proposed modulator is confirmed for such geometrical parameters. However, it is obvious that the TE propagation loss in the off-state is much higher than that of the TM polarization when w =320 nm and $h = 240$ nm. This is due to the fact that by w decreasing, the effect of the sidewall stack layers on the TE optical mode is stronger so that the total propagation loss of the TE mode is enhanced. It is interesting that by decreasing the width of the waveguide the obtained modulation depth for the TE polarization grows from 0.932 dB/μm to 2 dB/μm in the accumulation mode that is desirable, although the polarization-insensitivity is not guaranteed in this case. Therefore, although the enhanced modulation depth of the TE mode is of interest, the difference between the $\alpha_{\rm TE}$ and $\alpha_{\rm TM}$ specially at the ENZ point (off-state) also increases that is not favorable as the polarization-insensitivity of the structure is lost. Consequently, the optimized geometrical size of the waveguide should be investigated to achieve the highest modulation depth while keeping the polarization-insensitivity of the modulator. Another point to note is that as shown in Fig. 7(a), the propagation loss shows a relative maximum point at $N_{\rm ITO} \approx 4 \times 10^{20}{\rm cm}^{-3}$, which is related to the entry of the top and bottom graphene sheets into the high-loss region. Also, there is an absolute maximum point corresponding to the ENZ point at $N_{\rm ITO} = 6.48 \times 10^{20}{\rm cm}^{-3}$, at which the ITO reaches its maximum loss.

The variation of the propagation loss as a function of the Si core width at the ENZ carrier concentration of ITO ($N_{\rm ITO} = 6.48 \times 10^{20}{\rm cm}^{-3}$) is shown in Fig. 7(b). As it is seen, the propagation loss of the TE mode is highly affected by the Si core width while that of the TM mode is nearly unchanged. Generally, there is a reduction of propagation loss by increasing the core width because of the weaker effect of ITO layer at the sidewalls. The propagation loss of the TE mode at the off-state below the Si core width of 300 nm is more than 3 dB/μm. However, there is a significant difference between the $\alpha_{\rm TE}$ and $\alpha_{\rm TM}$ that makes the modulator polarization-dependent. According to Fig. 7(b), the Si core width of about 380 nm ensures the polarization-insensitivity of the modulator where $\alpha_{\rm TE}$ and $\alpha_{\rm TM}$ at the off-state is approximately 0.935 dB/μm.

According to Fig. 1, the proposed structure is also covered by a Si clad layer that can improve the performance of the modulator. The effects of the thickness of the Si clad layer on different characteristics of the modulator including the modulation depth, insertion loss, reflection and figure of merit (FOM) are plotted in Figs. 8(a) and 8(b) for both TE and TM polarizations, respectively. It is obvious that the modulation depth of both the TE and TM modes increase by increasing the thickness of the clad. This is due to the fact that thicker Si clad yields more confinement of light into the deposited stack layers so that the ITO-light interaction is enhanced and higher modulation depth is expected. Consequently, the FOM of the modulator that is defined as ${\rm FOM} = \frac{\alpha_{\rm off} - \alpha_{\rm on}}{\alpha_{\rm on}}$ increases too. It is interesting that FOMs in the order of more than 1800 is attainable that is two orders of magnitude larger than that is reported in Ref. [18]. As

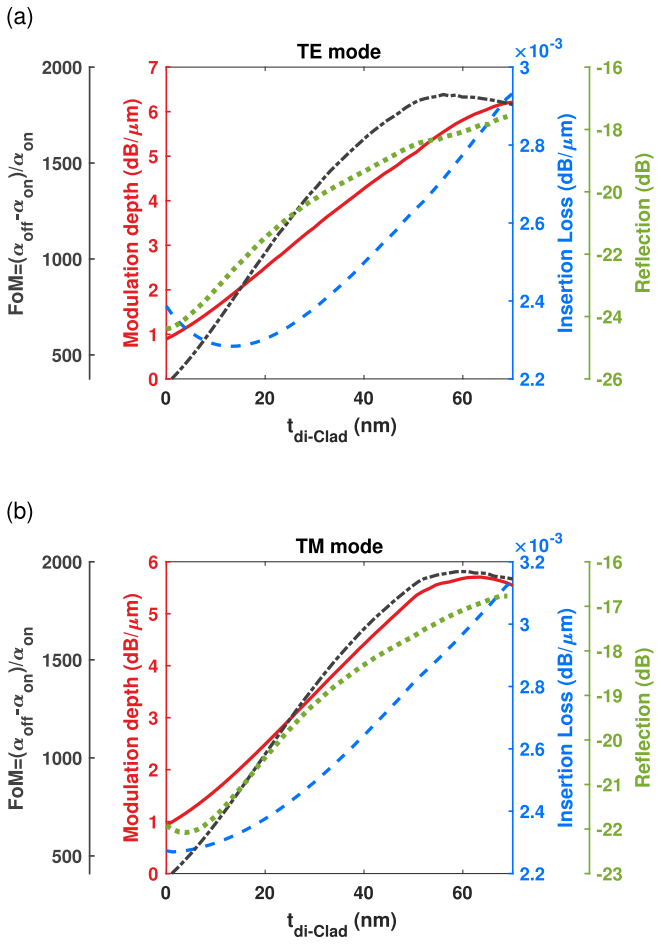

Fig. 8. The modulation depth, insertion loss, FOM and reflection of the proposed modulator versus the thickness of the Si clad layer for the fundamental (a) TE and (b) TM modes.

it is shown in Fig. 8(a), as the thickness of the clad increases to 20 nm, the insertion loss (including all loss mechanisms such as material loss, reflection at the waveguide-modulator interface, and power escaped from the modulator) of the TE mode decreases down to about 2.3×10^{-3} dB/μm. In fact, when the thickness of the clad increases, the optical loss associated with the out-of-plane radiation is reduced and less optical power can escape the waveguide. However, as it can be seen in Fig. 8(a), by further increasing the thickness, the insertion loss rises because the propagating light is more confined to the stack layers so that its interaction with the ITO and graphene layers is enhanced that results in higher insertion loss. Almost similar behavior is also seen in Fig. 8(b) that is the calculated insertion loss of the TM mode. The ultra-low insertion losses of both the TE and TM modes in the order of 2×10^{-3} dB/μm that are much lower than those previously reported [18]–[20] are other outstanding achievements of our proposed modulator. Finally, the calculated reflection from the structure as a result of the coupling from the input waveguide to the modulator is depicted in Fig. 8. It is generally obvious that thicker Si clad layer yields more reflection from the modulator. This is because by increasing the thickness of the clad, the effective index of the propagating mode increases and consequently higher index mismatch between the

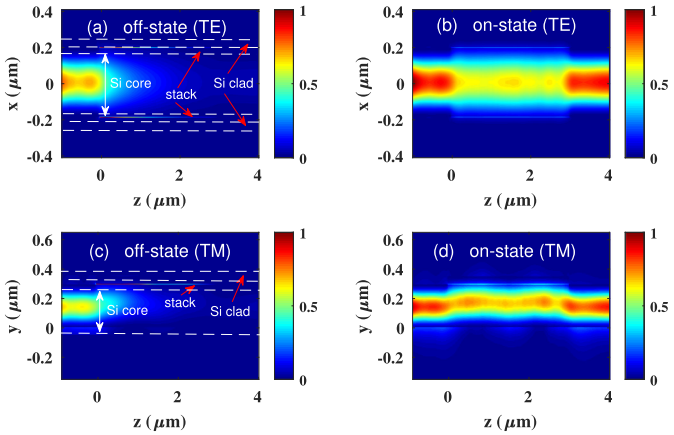

Fig. 9. The electric field distributions in the x-z and y-z planes of the modulator. The electric field profiles of the propagating TE polarization in the (a) off- and (b) on-states. The corresponding profiles of the propagating TM polarization when the modulator is in the (c) off- and (d) on-states.

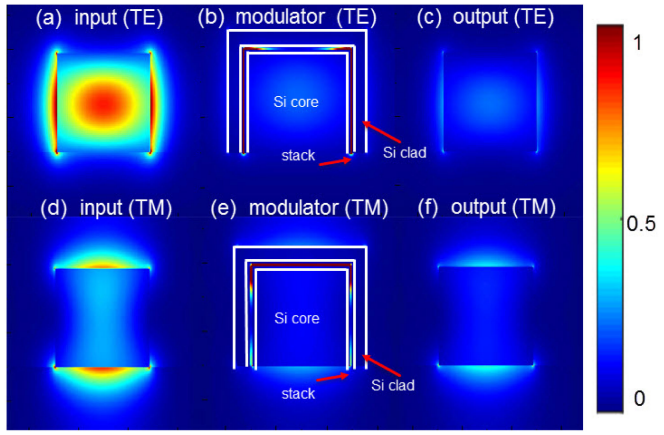

Fig. 10. The electric field profiles of fundamental TE and TM modes. The electric field profiles ($|\boldsymbol{E}|$) of the fundamental TE mode (a) in the input Si waveguide (b) in the middle of the modulator, and (c) in the output Si waveguide. The $|\boldsymbol{E}|$ field profile of fundamental TM mode (d) in the input of Si waveguide (e) in the middle of the modulator, and (f) in the output of Si waveguide.

input coupling waveguide and modulator is expected. However, it should be mentioned that the amount of reflection is negligible to affect the high performance of the structure.

The most advantage of utilizing a Si-clad layer is that it can remarkably increase the modulation depth. As can be seen in Figs. 8(a) and 8(b), by increasing the Si-clad thickness from 0 to 55 nm, the modulation depth is enhanced from 0.932 dB/μm to 5.23 dB/μm (from 0.947 dB/μm to 5.36 dB/μm) for the TE (TM) polarization. It should be noted that although a further increase in the thickness of the clad layer can increase the modulation depth, on the other hand, it can lead to the excitation of higher-order modes of the modulator. To prevent this, we consider the Si-clad thickness of 55 nm.

Finally, in order to demonstrate the operation of the modulator, the propagation of the light along the proposed structure is simulated using the 3D FDTD method. The profiles of the electric field intensities at the wavelength of 1550 nm for different states of the modulator are depicted in Fig. 9. The electric field intensities of the TE polarization in the off- and on-states of the modulator are shown in Figs. 9(a) and 9(b), respectively. As it is seen in Fig. 9(a), the propagating TE light experiences significant loss when the ITO layer is set at the ENZ point (off-state). It is while the insertion loss of the structure is negligible when the modulator is in the on-state that is shown in Fig. 9(b). On the other side, the electric field profiles of the TM polarization in the off- and on-states are also shown in Figs. 9(c) and 9(d), respectively. As it is shown, the operation of the modulator is similar to the TE polarization which confirm the polarization-insensitivity of the structure. Consequently, the polarization-insensitivity, the high modulation depth, the low insertion loss, the extraordinary FOM and the low required voltage of our proposed graphene-based modulator could be very promising for high performance optical communication networks.

Moreover, the mode profiles in the input Si waveguide, in the middle of the modulator, and in the output Si waveguide at the off-state are shown in Figs. 10(a)-(c) and Figs. 10(d)-(f) for the TE and TM modes, respectively. As can be seen in Figs. 10(b) and (e), the most portion of the passing optical power is localized in the ITO layer and undergoes extreme losses. It should be noted that the structure of the modulator can be effectively considered as a HLH (H=high refractive index, L=low refractive index) stack, in which a thin ITO layer (with $\varepsilon_{\mathrm{ITO}} \approx 0$ at ENZ point) is sandwiched between Si core waveguide and Si clad layer (with $\varepsilon_{\mathrm{Si}} = 11.94$). Due to the continuity of the perpendicular components of the electric displacement ($\boldsymbol{D} = \varepsilon \boldsymbol{E}$) at the interface of the HLH stack ($\varepsilon_{\mathrm{Si}} \boldsymbol{E}_{\mathrm{H}} = \varepsilon_{\mathrm{ITO}} \boldsymbol{E}_{\mathrm{L}}$), and due to $\varepsilon_{\mathrm{Si}} \gg \varepsilon_{\mathrm{ITO}}$ at ENZ point, it can be seen that the most portion of the optical field is localized in the ITO layer ($\boldsymbol{E}_{\mathrm{Si}} \ll \boldsymbol{E}_{\mathrm{ITO}}$).

V. Conclusion

In summary, we design an ENZ electro-absorption modulator based on a stack of three-layer graphene and ITO. The structure is simulated using the 3D FDTD method and the operation of the modulator is investigated. According to the presented results, when an external voltage of as low as 3.42 V is applied across the graphene layers, the carrier concentration of the ITO layer is adjusted to the ENZ point and the graphene layers become lossy so that the modulator is set to the off-state. As a result, a modulation depth of about 5.3 dB/μm is obtained for both the TE and TM polarization. It is interesting that when the modulator is in the on-state, the insertion loss is as low as 2.5×10^{-3} dB/μm that is attributed to the Si clad covering the whole stack. Consequently, a very high FOM of more than 1800 is calculated that to the best of our knowledge is the highest value ever reported. The synergistic effect obtained by simultaneous modulation of the ITO and graphene losses has played an important role to achieve such outstanding characteristics. Therefore, such promising features make our proposed modulator a promising candidate for optical communication systems.

References

[1] R. Soref and B. Bennett, "Electrooptical effects in silicon," *IEEE J. Quantum Electron.*, vol. QE-23, no. 1, pp. 123–129, Jan. 1987.

[2] K. Liu, C. R. Ye, S. Khan, and V. J. Sorger, "Review and perspective on ultrafast wavelength-size electro-optic modulators," *Laser Photon. Rev.*, vol. 9, no. 2, pp. 172–194, 2015.

[3] Q. Xu, B. Schmidt, S. Pradhan, and M. Lipson, "Micrometre-scale silicon electro-optic modulator," *Nature*, vol. 435, no. 7040, pp. 325–327, 2005.

[4] L. Mastronardi *et al.*, "High-speed Si/GeSi hetero-structure electro absorption modulator," *Opt. Exp.*, vol. 26, no. 6, pp. 6663–6673, 2018.

[5] G. T. Reed, G. Mashanovich, F. Y. Gardes, and D. J. Thomson, "Silicon optical modulators," *Nat. Photon.*, vol. 4, no. 8, pp. 518–526, 2010.

[6] J. T. Kim, K. H. Chung, and C.-G. Choi, "Thermo-optic mode extinction modulator based on graphene plasmonic waveguide," *Opt. Exp.*, vol. 21, no. 13, pp. 15280–15286, 2013.

[7] G. Cocorullo, M. Iodice, and I. Rendina, "All-silicon Fabry-Perot modulator based on the thermo-optic effect," *Opt. Lett.*, vol. 19, no. 6, p. 420–422, 1994.

[8] W. E. Ross, D. Psaltis, and R. H. Anderson, "Two-dimensional magneto-optic spatial light modulator for signal processing," *Opt. Eng.*, vol. 22, 1983, Art no. 224485.

[9] M. Streshinsky *et al.*, "Low power 50 gb/s silicon traveling wave mach-zehnder modulator near 1300 nm," *Opt. Exp.*, vol. 21, no. 25, pp. 30350–30357, 2013.

[10] P. Dong, L. Chen, and Y. kai Chen, "High-speed low-voltage single-drive push-pull silicon Mach-Zehnder modulators," *Opt. Exp.*, vol. 20, no. 6, pp. 6163–6169, 2012.

[11] M. Li, L. Wang, X. Li, X. Xiao, and S. Yu, "Silicon intensity machzehnder modulator for single lane 100gb/s applications," *Photon. Res.*, vol. 6, no. 2, pp. 109–116, 2018.

[12] R. Amin *et al.*, "Active material, optical mode and cavity impact on nanoscale electro-optic modulation performance," *Nanophotonics*, vol. 7, no. 2, pp. 455–472, 2018.

[13] U. Koch, C. Hoessbacher, J. Niegemann, C. Hafner, and J. Leuthold, "Digital plasmonic absorption modulator exploiting epsilon-near-zero in transparent conducting oxides," *IEEE Photon. J.*, vol. 8, no. 1, pp. 1–13, Feb. 2016.

[14] V. J. Sorger, N. D. Lanzillotti-Kimura, R.-M. Ma, and X. Zhang, "Ultra-compact silicon nanophotonic modulator with broadband response," *Nanophotonics*, vol. 1, no. 1, pp. 17–22, 2012.

[15] R. Amin *et al.*, "Sub-wavelength GHz-fast broadband ITO machzehnder modulator on silicon photonics," *Optica*, vol. 7, no. 4, pp. 333–335, 2020.

[16] C. Ye, S. Khan, Z. R. Li, E. Simsek, and V. J. Sorger, "λ-size ITO and graphene-based electro-optic modulators on SOI," *IEEE J. Sel. Topics Quantum Electron.*, vol. 20, no. 4, Jul./Aug. 2014, Art. no. 3400310.

[17] M. G. Wood *et al.*, "Gigahertz speed operation of epsilon-near-zero silicon photonic modulators," *Optica*, vol. 5, no. 3, pp. 233–236, 2018.

[18] S. Zhu, G. Q. Lo, and D. L. Kwong, "Design of an ultra-compact electro-absorption modulator comprised of a deposited TiN/HfO_2/ITO/Cu stack for CMOS backend integration," *Opt. Exp.*, vol. 22, no. 15, pp. 17930–17947, 2014.

[19] Z. Lu, W. Zhao, and K. Shi, "Ultracompact electroabsorption modulators based on tunable epsilon-near-zero-slot waveguides," *IEEE Photon. J.*, vol. 4, no. 3, pp. 735–740, Jun. 2012.

[20] Y. Kuang, Y. Liu, L. Tian, W. Han, and Z. Li, "A dual-slot electro-optic modulator based on an epsilon-near-zero oxide," *IEEE Photon. J.*, vol. 11, no. 4, pp. 1–12, Aug. 2019.

[21] C.-H. Liu, Y.-C. Chang, T. B. Norris, and Z. Zhong, "Graphene photodetectors with ultra-broadband and high responsivity at room temperature," *Nat. Nanotechnol.*, vol. 9, no. 4, pp. 273–278, 2014.

[22] F. Xia, T. Mueller, Y.-m. Lin, A. Valdes-Garcia, and P. Avouris, "Ultrafast graphene photodetector," *Nat. Nanotechnol.*, vol. 4, no. 12, pp. 839–843, 2009.

[23] M. Heidari *et al.*, "A high-performance TE modulator/TM-pass polarizer using selective mode shaping in a VO_2-based side-polished fiber," *Nanophotonics*, vol. 10, 2021, Art. no. 20210225.

[24] Q. Bao *et al.*, "Broadband graphene polarizer," *Nat. Photon.*, vol. 5, no. 7, pp. 411–415, 2011.

[25] Z. Sun *et al.*, "Graphene mode-locked ultrafast laser," *ACS Nano*, vol. 4, no. 2, pp. 803–810, 2010.

[26] S. Bahadori-Haghighi, R. Ghayour, and M. H. Sheikhi, "Three-dimensional analysis of an ultrashort optical cross-bar switch based on a graphene plasmonic coupler," *J. Light. Technol.*, vol. 35, no. 11, pp. 2211–2217, 2017.

[27] S. Bahadori-Haghighi, R. Ghayour, and A. Zarifkar, "Tunable graphene dielectric metasurfaces for terahertz all-optical modulation," *J. Appl. Phys.*, vol. 128, no. 4, pp. 044506–044515, 2020.

[28] M. Heidari and V. Ahmadi, "Design and analysis of a graphene magneto-plasmon waveguide for plasmonic mode switch," *IEEE Access*, vol. 7, pp. 43406–43413, 2019.

[29] B. Janjan, M. Miri, D. Fathi, M. Heidari, and D. Abbott, "Hybrid Si_3N_4/VO_2 modulator thermally triggered by a graphene microheater," *IEEE J. Sel. Topics Quantum Electron.*, vol. 26, no. 5, Sep./Oct. 2020, Art. no. 3400206.

[30] M. Sadeghi, B. Janjan, M. Heidari, and D. Abbott, "Mid-infrared hybrid Si/VO_2 modulator electrically driven by graphene electrodes," *Opt. Exp.*, vol. 28, no. 7, pp. 9198–9207, 2020.

[31] K. Bolotin *et al.*, "Ultrahigh electron mobility in suspended graphene," *Solid State Commun.*, vol. 146, no. 9-10, pp. 351–355, 2008.

[32] S. Bahadori-Haghighi, R. Ghayour, and M. H. Sheikhi, "Design and analysis of low loss plasmonic waveguide and directional coupler based on pattern-free suspended graphene sheets," *Carbon*, vol. 129, pp. 653–660, 2018.

[33] A. Pospischil *et al.*, "CMOS-compatible graphene photodetector covering all optical communication bands," *Nat. Photon.*, vol. 7, pp. 892–896, 2013.

[34] M. Liu *et al.*, "A graphene-based broadband optical modulator," *Nature*, vol. 474, no. 7349, pp. 64–67, 2011.

[35] M. Liu, X. Yin, and X. Zhang, "Double-layer graphene optical modulator," *Nano Lett.*, vol. 12, no. 3, pp. 1482–1485, 2012.

[36] H. Dalir, Y. Xia, Y. Wang, and X. Zhang, "Athermal broadband graphene optical modulator with 35 GHz speed," *ACS Photon.*, vol. 3, no. 9, pp. 1564–1568, 2016.

[37] C. Qiu, W. Gao, R. Vajtai, P. M. Ajayan, J. Kono, and Q. Xu, "Efficient modulation of 1.55 μm radiation with gated graphene on a silicon microring resonator," *Nano Lett.*, vol. 14, no. 12, pp. 6811–6815, 2014.

[38] X. Hu and J. Wang, "Design of graphene-based polarization-insensitive optical modulator," *Nanophotonics*, vol. 7, no. 3, pp. 651–658, 2018.

[39] Y. Xu *et al.*, "Hybrid graphene-silicon based polarization-insensitive electro-absorption modulator with high-modulation efficiency and ultra-broad bandwidth," *Nanomater.*, vol. 9, no. 2, pp. 157–172, 2019.

[40] S. Li *et al.*, "Nanometre-thin indium tin oxide for advanced high-performance electronics," *Nat. Mater.*, vol. 18, no. 10, pp. 1091–1097, 2019.

[41] Z. Ma, Z. Li, K. Liu, C. Ye, and V. J. Sorger, "Indium-tin-oxide for high-performance electro-optic modulation," *Nanophotonics*, vol. 4, no. 2, pp. 198–213, 30 Jun. 2015.

[42] I. C. Reines, M. G. Wood, T. S. Luk, D. K. Serkland, and S. Campione, "Compact epsilon-near-zero silicon photonic phase modulators," *Opt. Exp.*, vol. 26, no. 17, pp. 21594–21605, 2018.

[43] A. Melikyan *et al.*, "Surface plasmon polariton absorption modulator," *Opt. Exp.*, vol. 19, no. 9, pp. 8855–8869, 2011.

[44] R. Amin *et al.*, "A deterministic guide for material and mode dependence of on-chip electro-optic modulator performance," *Solid State Electron*, vol. 136, pp. 92–101, 2017.

[45] J. Xia, F. Chen, J. Li, and N. Tao, "Measurement of the quantum capacitance of graphene," *Nat. Nanotechnol.*, vol. 4, no. 8, pp. 505–509, 2009.

[46] L. Alloatti *et al.*, "Second-order nonlinear optical metamaterials: Abc-type nanolaminates," *Appl. Phys. Lett.*, vol. 107, no. 12, 2015, Art no. 121903.

[47] A. Pachoud, M. Jaiswal, P. K. Ang, K. P. Loh, and B. Özyilmaz, "Graphene transport at high carrier densities using a polymer electrolyte gate," *EPL*, vol. 92, no. 2, pp. 2700-1–127001-6, 2010.

[48] F. Giubileo and A. D. Bartolomeo, "The role of contact resistance in graphene field-effect devices," *Prog. Surf. Sci*, vol. 92, no. 3, pp. 143–175, 2017.

[49] S. M. Song, J. K. Park, O. J. Sul, and B. J. Cho, "Determination of work function of graphene under a metal electrode and its role in contact resistance," *Nano Lett.*, vol. 12, no. 8, pp. 3887–3892, 2012.

[50] M. Heidari and V. Ahmadi, "Graphene-based mid-infrared plasmonic isolator with multimode interferometer," *Opt. Lett.*, vol. 45, no. 20, pp. 5764–5767, 2020.

Mohsen Heidari was born in Shiraz, Iran, in 1989. He is currently a Research Associate with the Department of Electrical and Electronic Engineering, Tarbiat Modares University, Tehran, Iran. His current research interests include graphene and 2D materials-based plasmonic and magneto-plasmonic, all-optical switches and modulators, plasmonic isolators, nanophotonic devices, biosensors, quantum computing, and quantum communications.

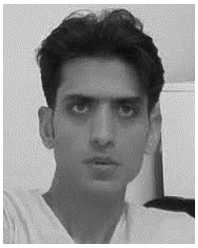

Shahram Bahadori-Haghighi was born in Shiraz, Iran, on August 6, 1986. He received the first honor in all his educational degrees. He is currently a Research Associate with the School of Electrical Engineering, Shiraz University, Shiraz, Iran. His research interests include integrated optics, nanoelectronics, and nonlinear optics.

Babak Janjan was born in Nahavand, Iran, on February 1989. He received the B.Sc. degree in electrical engineering from Isfahan University, Isfahan, Iran, in 2012, the M.Sc. degree in electrical engineering from Shiraz University, Shiraz, Iran, in 2015, and the Ph.D. degree in electrical engineering from Tarbiat Modares University, Tehran, Iran, in 2020. His current research interests include integrated optics and nonlinear optics.

Mohammad R. Khosravi received the B.Sc., M.Sc., and Ph.D. degrees in electrical engineering with expertise in communications and signal processing. He is currently with the Department of Electrical and Electronic Engineering Engineering, Shiraz, Iran. His main research interests include optical and radar imaging, digital image processing, remote sensing systems, computer communications, cyber-physical systems, internet of things, and industrial sensor networks.

Derek Abbott (Fellow, IEEE) was born in South Kensington, London, U.K., in 1960. He received the B.Sc. degree (Hons.) in physics from Loughborough University, Loughborough, U.K., in 1982 and the Ph.D. degree in electrical and electronic engineering from The University of Adelaide, Adelaide, SA, Australia, in 1997, under the supervision of K. Eshraghian and B. R. Davis. His research interests include multidisciplinary physics and electronic engineering applied to complex systems. His research programs span a number of areas of stochastics, game theory, photonics, energy policy, biomedical engineering, and computational neuroscience. He is a Fellow of the Institute of Physics, U.K., and an Honourary Fellow of Engineers Australia.

He was the recipient of a number of awards, including the South Australian Tall Poppy Award for Science, in 2004, the Australian Research Council Future Fellowship, in 2012, the David Dewhurst Medal, in 2015 the Barry Inglis Medal, in 2018, and the M. A. Sargent Medal for eminence in engineering, in 2019. He was the Editor and/or a Guest Editor for a number of journals, including the IEEE JOURNAL OF SOLID-STATE CIRCUITS, *Journal of Optics B*, *Chaos*, *Fluctuation and Noise Letters*, PROCEEDINGS OF THE IEEE, and the IEEE PHOTONICS JOURNAL. He has served on the Board of the PROCEEDINGS OF THE IEEE, and is currently on the Editorial Boards of the *Scientific Reports* (Nature), *Royal Society OS*, *Frontiers in Physics,* and IEEE ACCESS. He serves on the IEEE Publication Services and Products Board (PSPB) and is the current Editor-in-Chief (EIC) of IEEE ACCESS.